Earth and Planetary Science Letters 513 (2019) 40–50

Contents lists available at ScienceDirect

Earth and Planetary Science Letters

www.elsevier.com/locate/epsl

Heterogeneous upper mantle structure beneath the Ross Sea Embayment and Marie Byrd Land, West Antarctica, revealed by P-wave tomography

Austin L. White-Gaynor [a,*], Andrew A. Nyblade [a], Richard C. Aster [b], Douglas A. Wiens [c], Peter D. Bromirski [d], Peter Gerstoft [d], Ralph A. Stephen [e], Samantha E. Hansen [f], Terry Wilson [g], Ian W. Dalziel [h], Audrey D. Huerta [i], J. Paul Winberry [i], Sridhar Anandakrishnan [a]

[a] Department of Geosciences, Pennsylvania State University, United States of America
[b] Department of Geosciences, Warner College of Natural Resources, Colorado State University, United States of America
[c] Department of Earth and Planetary Sciences, Washington University in St. Louis, United States of America
[d] Scripps Institution of Oceanography, University of California, United States of America
[e] Woods Hole Oceanographic Institution, United States of America
[f] Department of Geological Sciences, University of Alabama, United States of America
[g] School of Earth Sciences, Ohio State University, United States of America
[h] Jackson School of Geosciences, University of Texas at Austin, United States of America
[i] Department of Geological Sciences, Central Washington University, United States of America

ARTICLE INFO

Article history:
Received 29 July 2018
Received in revised form 16 January 2019
Accepted 10 February 2019
Available online xxxx
Editor: M. Ishii

Keywords:
Antarctica
Ross Sea Embayment
West Antarctic Rift System
mantle structure
seismic tomography
Marie Byrd Land

ABSTRACT

We present an upper mantle P-wave velocity model for the Ross Sea Embayment (RSE) region of West Antarctica, constructed by inverting relative P-wave travel-times from 1881 teleseismic earthquakes recorded by two temporary broadband seismograph deployments on the Ross Ice Shelf, as well as by regional ice- and rock-sited seismic stations surrounding the RSE. Faster upper mantle P-wave velocities ($\sim +1\%$) characterize the eastern part of the RSE, indicating that the lithosphere in this part of the RSE may not have been reheated by mid-to-late Cenozoic rifting that affected other parts of the Late Cretaceous West Antarctic Rift System. Slower upper mantle velocities ($\sim -1\%$) characterize the western part of the RSE over a ~500 km-wide region, extending from the central RSE to the Transantarctic Mountains (TAM). Within this region, the model shows two areas of even slower velocities ($\sim -1.5\%$) centered beneath Mt. Erebus and Mt. Melbourne along the TAM front. We attribute the broader region of slow velocities mainly to reheating of the lithospheric mantle by Paleogene rifting, while the slower velocities beneath the areas of recent volcanism may reflect a Neogene-present phase of rifting and/or plume activity associated with the formation of the Terror Rift. Beneath the Ford Ranges and King Edward VII Peninsula in western Marie Byrd Land, the P-wave model shows lateral variability in upper mantle velocities of $\pm 0.5\%$ over distances of a few hundred km. The heterogeneity in upper mantle velocities imaged beneath the RSE and western Marie Byrd Land, assuming no significant variation in mantle composition, indicates variations in upper mantle temperatures of at least 100 °C. These temperature variations could lead to differences in surface heat flow of $\sim \pm 10$ mW/m^2 and mantle viscosity of 10^2 Pa s regionally across the study area, possibly influencing the stability of the West Antarctic Ice Sheet by affecting basal ice conditions and glacial isostatic adjustment.

1. Introduction

Over the past two decades, substantial progress has been made in deploying temporary broadband seismic stations throughout Antarctica, leading to many advances in our understanding of crustal and mantle structure across much of the continent. With improved seismic data coverage, it has become clear that there

* Corresponding author.
E-mail address: alw361@psu.edu (A.L. White-Gaynor).

https://doi.org/10.1016/j.epsl.2019.02.013
0012-821X/

is significantly more heterogeneity in West Antarctic (WA) upper mantle structure than earlier, lower resolution seismological studies of the region suggested (e.g., Masters et al., 1996; Danesi and Morelli, 2001; Ritzwoller et al., 2001). For example, data from the POLENET network have illuminated differences in crustal and upper mantle structure beneath the Marie Byrd Land (MBL) crustal block and portions of the central West Antarctic Rift System (WARS) (Hansen et al., 2014; Chaput et al., 2014; Lloyd et al., 2015; Heeszel et al., 2016; Shen et al., 2018) (Fig. 1), while data from the TAMSEIS and TAMNNET networks have illuminated heterogeneous structure beneath WA adjacent to the boundary with East Antarctica (EA) (e.g., Watson et al., 2006; Lawrence et al., 2006; Brenn et al., 2017; Graw et al., 2016).

Further characterizing the nature of heterogeneous WA upper mantle structure is not only important for advancing our understanding of the thermo-tectonic state of the crust and upper mantle but also for unraveling the geodynamic history of the WARS. In addition, it can provide improved constraints on surface heat flow and mantle viscosity, particularly if the heterogeneity is caused by variations in mantle temperature, and consequently help in estimating future sea level rise. Mantle viscosity affects glacial isostatic adjustment, and both glacial isostatic adjustment and surface heat flow can influence the response of ice sheets to climactic forcings (Gomez et al., 2015; Barletta et al., 2018).

Improved data coverage over a large portion of WA not included within the footprints of previous networks (e.g., TAMSEIS, TAMNNET, and POLENET) has recently been provided by the coupled RIS (Mantle Structure and Dynamics of the Ross Sea from a Passive Seismic Deployment on the Ross Ice Shelf) and DRIS (Dynamic Response of the Ross Ice Shelf to Wave-Induced Vibrations) projects. The RIS/DRIS network was deployed primarily on the floating ice of the Ross Ice Shelf between 2014–2017 and spanned much of the Ross Sea Embayment (RSE) (Fig. 1). In this study, we used data from the RIS/DRIS deployment and from several other networks (Fig. 1) to image the P-wave velocity structure of the upper mantle under the RSE and surrounding areas. Our P-wave model has improved spatial resolution compared to many previously published models (e.g., Ritzwoller et al., 2001; Danesi and Morelli, 2001; Sieminski et al., 2003 and references therein), revealing new regions of heterogeneity within the WA upper mantle, as well as providing enhanced resolution of heterogeneous structure initially identified in previous studies (e.g., Hansen et al., 2014; Heeszel et al., 2016). We attribute the imaged heterogeneity in upper mantle structure primarily to changes in mantle temperature, discuss how those changes could result from the history of rifting in WA, and examine the implications of those changes for surface heat flow and mantle viscosity.

2. Geologic setting

The Antarctic continent is composed of EA, a large Precambrian shield, and WA, which consists of several crustal blocks within a wide region of extended crust (Fig. 1; Dalziel and Elliot, 1982). Separating EA from WA are the ~3500 km-long, 4 km-high Transantarctic Mountains (TAM) (Fitzgerald, 2002). The EA-WA lithospheric boundary has experienced numerous periods of subduction, transpression, and extension since the Neoproterozoic (Fitzgerald, 2002). The TAM principally consist of metamorphic basement rocks deformed during the Cambrian-Ordovician Ross Orogeny overlain by thick, undeformed Devonian to Triassic Beacon Supergroup sediments (Fitzgerald, 2002). Major uplift of the TAM is thought to have initiated in the Paleogene (Fitzgerald, 1992).

Bounding the EA margin of the northern TAM within Northern Victoria Land is the Wilkes Subglacial Basin, a ~400 km-wide depression with mean bedrock elevations ~500 m below sea level (Fig. 1). Several models have been proposed for the origin of the Wilkes Subglacial Basin (e.g., Ferraccioli et al., 2009 and references therein), and its geodynamics are of broad interest because of the potential for substantial continental ice mass loss from the basin (Rignot et al., 2008).

MBL and the RSE sector of the WARS make up the majority of the WA portion of the study area (Fig. 1). MBL is the largest crustal block in WA and contains numerous Cenozoic volcanic centers that underlie, and in some cases protrude through the West Antarctic Ice Sheet. Outcrops near the coast indicate that the regional basement is composed of lowermost Paleozoic metamorphosed granitic rocks intruded by Devonian through Cretaceous magmas (Mukasa and Dalziel, 2000). Oligocene to Holocene alkaline volcanics associated with rifting of the WARS dominate most of the interior outcrops (LeMasurier, 1990); however, some lavas within a region of MBL have isotopic and trace elemental signatures that suggest a mantle source with a residual subduction component (LeMasurier et al., 2016). Proposed mechanisms for melt generation include a mantle plume, an upper mantle hotspot related to past subduction, and slab delamination (LeMasurier et al., 2016; LeMasurier and Landis, 1996; Finn et al., 2005). A region of seismicity arising from magmatic activity has been observed in MBL beneath the Executive Committee Range (Lough et al., 2013), and a second possible region has been identified in the King Edward VII Peninsula (KEP; Fig. 1) (Winberry and Anandakrishnan, 2003).

While there is some indication that rifting in WA began in the Jurassic, along with the emplacement of the Karoo-Ferrar Large Igneous Province, the primary phase of crustal extension occurred in the Late Cretaceous during the breakup of Gondwana (Siddoway, 2008). A second pulse of extension is thought to have occurred along the TAM margin in the Cenozoic, coeval with a period of TAM uplift and volcanism along the TAM margin near Ross Island (Fig. 1) (Fitzgerald, 2002).

The Ross Ice Shelf overlays much of the RSE sector of the WARS, which consists of a series of Late Cretaceous asymmetric grabens, including the Eastern Basin, Central Trough, Victoria Land Basin, and Northern Basin (Fig. 1) (Davey and Brancolini, 1995). The Eastern Basin spans the region east of 180° longitude in the embayment, from the continental slope southward beneath the Ross Ice Shelf (Davey, 1981). The western portion of the RSE, closer to the TAM boundary, is composed of the Central Trough, Victoria Land Basin, and Northern Basin, hereafter referred to as the western basins. The Victoria Land Basin has been associated with a pulse of extension during the Paleogene (Fitzgerald, 2002; Fielding et al., 2006). Post-Oligocene (Neogene) rifting is thought to have occurred within the narrow Terror Rift, which lies within the Victoria Land Basin, and is possibly associated with transtension and seafloor spreading (Fig. 1) (Granot et al., 2013; Fielding et al., 2006) or the impingement of a mantle plume (Phillips et al., 2018).

3. Previous geophysical studies

The first continental-scale tomographic images of the upper mantle beneath Antarctica, extracted from global surface wave tomography models and constrained by only a few observations in Antarctica, showed fast upper mantle velocities beneath much of the continent (Roult et al., 1994; Masters et al., 1996). By adding data from additional permanent seismic stations in Antarctica, a next generation of continental-scale surface wave models achieved improved resolution and identified a dichotomy in the Antarctic upper mantle structure, with fast velocities beneath EA and slow velocities beneath WA (Ritzwoller et al., 2001; Danesi and Morelli, 2001; Sieminski et al., 2003).

Many of the earliest geophysical investigations of the WARS seeking regional-scale resolution of crustal and upper mantle structure were based on marine and aerogeophysical surveys (e.g.,

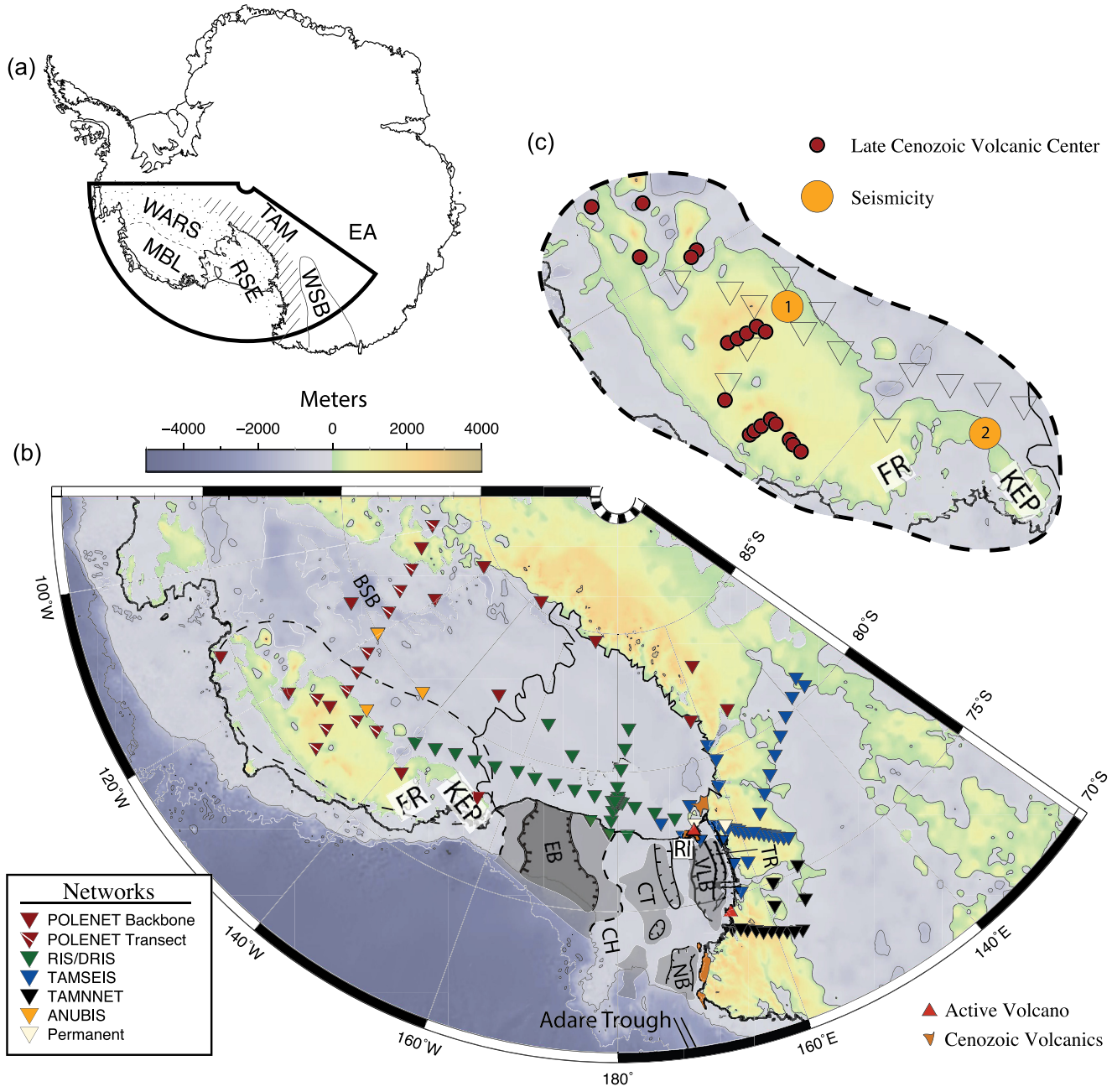

Fig. 1. a) Generalized tectonic map of the study region. Transantarctic Mountains (TAM) are denoted with parallel line segments (Dalziel and Elliot, 1982). The Marie Byrd Land (MBL) crustal block (Dalziel and Elliot, 1982) and the Wilkes Subglacial Basin (WSB) are outlined by the dotted and solid lines. The West Antarctic Rift System (WARS) is lightly shaded. RSE: Ross Sea Embayment, EA: East Antarctica. b) Map showing the locations of seismic stations used in this study. Topography is from BEDMAP2 (Fretwell et al., 2013). RI: Ross Island, FR: Ford Ranges, KEP: King Edward VII Peninsula, BSB: Byrd Subglacial Basin. Boundaries for the Eastern Basin (EB) are compiled from several sources (Decesari et al., 2007; Davey and Brancolini, 1995; Brancolini et al., 1995) with the outermost limit shown by the dotted lines and the inner most limit shown by the solid lines. Shaded regions denoting the Central Trough (CT), Victoria Land Basin (VLB), and Northern Basin (NB) are from Brancolini et al. (1995), while solid outlines denoting the CT, VLB, NB, and Terror Rift (TR) are from Granot et al. (2013). CH: Central High, RI: Ross Island. c) Map of the MBL crustal block (Dalziel and Elliot, 1982) showing locations of Cenozoic volcanoes (red circles; LeMasurier et al., 2016) and seismicity (orange circles) reported by (1) Lough et al. (2013) and (2) Winberry and Anandakrishnan (2003). Background topography is from BEDMAP2. (For interpretation of the colors in the figure(s), the reader is referred to the web version of this article.)

Behrendt et al., 1996; Trey et al., 1999; Karner et al., 2005). For example, Behrendt et al. (1996) reported evidence for Cenozoic volcanism, based on aeromagnetic signatures, extending from Ross Island toward the central RSE along reactivated Mesozoic faults. A crustal model derived from gravity observations in the RSE showed anti-correlation of gravity anomalies with many sedimentary basins, suggesting a two-phase rift history that differentiated the Eastern Basin, Central Trough, Victoria Land Basin and Northern Basin from the Terror Rift (Karner et al., 2005). Using data from a marine seismic refraction survey across the front of the Ross Ice Shelf, Trey et al. (1999) imaged P_n velocities of $\geq$8.0 km/s in the uppermost mantle across the RSE, with a reduction to ~7.8 km/s near Ross Island. Together, many of the regional-scale geophysical studies pointed to a degree of heterogeneity in the crust and upper mantle beneath WA not resolved in continental-scale tomography models.

Starting in the late 1990s, the development of portable broadband seismic stations led to a substantial improvement in Antarctic terrestrial seismic data coverage. From 2000–2003, the TAMSEIS project included 45 broadband seismic stations deployed from the

TAM front near Ross Island into EA. Using data from that project, Watson et al. (2006) imaged a sharp lithospheric boundary between EA and WA below the TAM. Since 2007, the POLENET project has operated a backbone network of seismic stations in EA and WA augmented with two temporary regional arrays (Fig. 1). Lloyd et al. (2015) used data from the POLENET stations to develop P- and S-wave tomography models that show a large-scale low velocity anomaly in the upper mantle beneath MBL and parts of the central WARS. Combining the POLENET and TAMSEIS data, continental-scale body wave (Hansen et al., 2014) and surface wave (Heeszel et al., 2016) tomography models imaged upper mantle structure more broadly beneath the WARS, but limited resolution in these models from a lack of stations in the RSE region make it difficult to determine if low velocity anomalies beneath MBL and Ross Island connect at upper mantle depths beneath the RSE.

The 2012–2015 deployment of the TAMNNET array in Northern Victoria Land provided additional data for imaging the WA-EA boundary, parts of the RSE around the Terror Rift and its active volcanic centers, and parts of the Wilkes Subglacial Basin (Brenn et al., 2017; Graw et al., 2016). Shen et al. (2018) combined the previous broadband datasets with the RIS/DRIS data to image the shear-wave velocity structure of the WA crust and upper mantle using receiver functions and Rayleigh waves from ambient noise and earthquakes. Their results show that both the lithosphere and crustal thickness is highly variable throughout the region, with thicker lithosphere in the eastern Ross Sea compared to the western Ross Sea. Ramirez et al. (2016, 2017), Chaput et al. (2014), and Lawrence et al. (2006) have also investigated crustal and upper mantle structure beneath these networks using a variety of techniques.

4. Data selection and preparation

The primary dataset used for this study comes from the RIS/DRIS network (https://doi.org/10.7914/SN/XH_2014), which consisted of a two-year deployment of 34 broadband seismometers (Fig. 1). The RIS project deployed 18 seismometers with ~80 km spacing across the Ross Ice Shelf parallel to the shelf coast, from Ross Island to MBL. The simultaneous DRIS project deployed 16 seismometers N-S along the center of the Ross Ice Shelf, parallel to ice flow, with ~5–20 km spacing. Because of the up to ~600 m water column underlying the Ross Ice Shelf, S-waves were not well recorded, and so we limit our investigation here to the use of teleseismic P-waves.

We also used data from 28 regional POLENET (https://doi.org/10.7914/SN/YT_2007) stations in the TAM, MBL, and the central WARS, 15 TAMNNET stations (https://doi.org/10.7914/SN/ZJ_2012) in Northern Victoria Land, and 35 TAMSEIS stations (https://doi.org/10.7914/SN/XP_2000) in the TAM and EA. In addition, data were used from two Antarctic Network of Unattended Broadband Seismometers (ANUBIS; https://doi.org/10.7914/SN/YI_1997), as well as from permanent Global Seismic Network stations SBA (https://doi.org/10.7914/SN/GT) and VNDA (https://doi.org/10.7914/SN/IU). In total, data from 116 stations were used, spanning a timeframe from 2001–2017 and ranging geographically from the EA craton, across the TAM and the Ross Ice Shelf, and throughout much of MBL and the WARS (Fig. 1; Supp. Table 1).

We gathered teleseismic P-waves for M ≥ 5.5 earthquakes at epicentral distances ranging from 30–90°. Vertical-component waveforms for 1881 events were corrected for instrument response and bandpass filtered between 0.5–5 Hz. We manually picked initial P-wave arrivals on all available traces for each event. More precise relative arrival times were then determined for events with three or more picks using the multichannel cross-correlation (MCCC) approach of VanDecar and Crosson (1990). This technique uses a three-second window around the initial picks and cross-correlates all combinations of traces for each event to find the ensemble correlation maxima. We accepted only cross-correlation coefficients of ≥0.70, with 93% (i.e., 1727) of the events meeting this threshold. A regularized least-squares optimization was used to find the best-fitting mean arrival time, from which cross-correlation coefficients and their distributions, as well as relative arrival times and data error, were calculated. Fig. 2 shows the locations of all events used in the final inversion, and event information can be found in Supplemental Table 2. It is important to note that uneven azimuthal source distribution can lead to a bias of the model in the direction of the denser source coverage. Fortunately, the dense source distribution from the Andean and Sumatran subduction zones led to an increased sensitivity in our model to structure roughly along strike of the linear portion of the RIS/DRIS deployment. The dataset yielded a total of 32,454 P-wave relative arrival times, with 11,381 (~35%) coming from the RIS/DRIS stations.

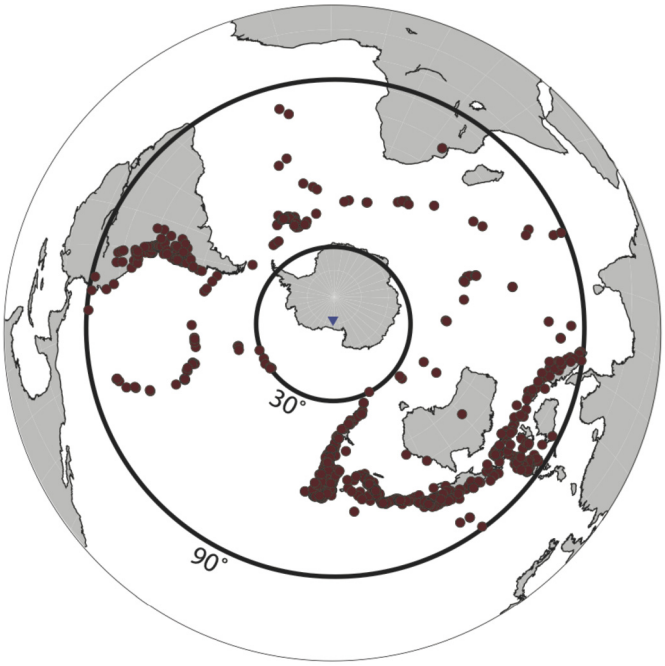

Fig. 2. Locations of M ≥ 5.5 earthquakes (red circles) used in this study plotted with respect to the center of the study area (inverted blue triangle).

5. Inversion of travel-time residuals

The relative P-wave arrival times were inverted for variations in mantle velocities using the VanDecar (1991) method, which employs a conjugate-gradient algorithm and simultaneously solves for 3D updates to model slowness, station static terms, and event relocation terms by reducing the misfit of travel-time residuals. The station terms account for shallow structure at depths that lack crossing ray paths (i.e., <50 km), and the event relocation terms absorb event location error and heterogeneous structure outside of the model domain. We incorporated smoothing and flattening regularization to stabilize the inversion.

The model domain for the inversion extended from 132°E to 97°W longitude, 67°S to 89°S latitude, and from the surface to 1600 km depth. Intersecting grid lines, or knots, were spaced 2° apart in longitude and 0.5° apart in latitude within the central portion of the model domain (i.e., between 72–83°S, 139°180°E, and 180–107°W; Supp. Fig. 1), with variable knot spacing at depth. Between the surface and 200 km depth, knots were spaced at 25 km, between 200–1200 km depth knots were spaced at 50 km, and between 1200–1600 km depth they were spaced at 100 km. Outside

this central region, knot spacing gradually increased in longitude and latitude, with the same vertical spacing as the central portion.

As first steps in the inversion method, we numerically calculated partial derivatives at each knot using slowness perturbations from the 1D IASP91 model (Kennett and Engdahl, 1991), and initial travel-time residuals were calculated relative to that velocity model. During the inversion process, models were then iteratively updated until changes in the model resulted in insignificant (<0.01 s) changes to the RMS travel-time residual. To select optimal smoothing and flattening parameters, we used a trade-off curve between the RMS travel-time residual reduction and the model roughness (Supp. Fig. 2).

6. Results

Model results are shown in Fig. 3, where the P-wave velocities (V_P) are plotted as percent differences relative to the model mean. Across MBL, a −0.75% V_P anomaly is observed between ∼75 and >500 km depth (Anomaly A; Fig. 3). There is some evidence that Anomaly A continues into the central WARS along the linear portion of the POLENET Transect array (Fig. 1); however, outside of this region, Anomaly A is located mainly beneath the area of Cenozoic volcanism in MBL (Fig. 3). In the regions surrounding Anomaly A, relatively fast (0.75% V_P) structure is present from ∼75–300 km depth. Anomaly B, a region of higher V_P (∼0.75%), separates Anomaly A from a region of lower V_P (Anomaly C) within the KEP (Fig. 3). Anomaly C is isolated laterally and is present to a depth of ∼400 km. Both Anomalies B and C are ∼200 km wide along-strike of the RIS/DRIS network.

Our model also shows clear differences in the upper mantle structure between the eastern and western RSE. The eastern RSE is associated with a ∼0.25% V_P anomaly in the upper 400 km of the model space (Anomaly D). This anomaly is ∼500 km wide, extending from the edge of the KEP to the center of the RSE. In the western RSE, a ∼500 km wide low V_P anomaly (−0.50%; Anomaly E) parallels the front of the TAM and is present down to ∼600 km depth. Within this broader low velocity region, three distinct areas of even lower V_P exist (Anomalies F, G, and H). Anomaly F is located in the central RSE, near the front of the Ross Ice Shelf, while Anomalies G and H are situated along the TAM boundary, directly beneath areas of recent and active volcanism (Fig. 1). In cross-section, Anomaly F is separated from Anomaly G by mantle with mean V_P structure (Fig. 3e); however, there is connectivity between Anomalies G and H along the Terror Rift (Fig. 3f). Anomalies F, G, and H are restricted to the upper 300 km of the model space.

A pronounced V_P gradient is present in our model under the TAM north of ∼80°S latitude. There is a ∼2.5% increase in V_P from the WARS to the EA flank of the TAM. Within EA, a ∼1.25% V_P anomaly (Anomaly I) is present between ∼50–500 km depth. All of EA has above average V_P except for the Wilkes Subglacial Basin. Anomaly J within the Wilkes Subglacial Basin has a peak anomalous V_P of −0.75% and is found north of ∼75°S latitude (Fig. 3).

The station static terms removed during the inversion process are positive for regions with slower and somewhat thinner than average crust (i.e., MBL, 27 km; Chaput et al., 2014; Ramirez et al., 2017) and negative in areas of faster and thicker than average crust (i.e., TAM, 42 km; Chaput et al., 2014; Ramirez et al., 2017). Where crustal thickness is much thinner than average (i.e., RSE, 19 km; Trey et al., 1999), station static corrections are relatively small (Supp. Fig. 3).

7. Resolution tests

7.1. Checkerboard tests

Model resolution was tested using a series of synthetic checkerboard tests (Fig. 4). We placed gaussian tapered spheres with peak amplitudes of ±5% and radii of 50 km and 100 km at depths of 100 km and 200 km, respectively. Travel times with added noise (4% standard deviation) were then calculated for the synthetic models and inverted to determine which parts of the model domain show the best recovery. For the 50 km radius spheres centered at 100 km depth, a majority of the checkers are recovered along the A–A′ transect (Fig. 4e). The model recovers roughly 10–15% of the initial amplitudes, with the best recovery around Ross Island (Fig. 4a–b). Vertical smearing is common in body wave tomography because of the vertical nature of the ray paths. On the A–A′ transect, vertical smearing of ∼100 km places peak amplitudes at ∼200 km depth rather than at the initial 100 km position (Fig. 4e). Likewise, for the 100 km radius spheres placed at 200 km depth (Fig. 4c–d, f), vertical smearing of ∼100 km occurs, resulting in peak amplitude (20–30%) recovery at ∼300 km depth. Amplitude recovery of the checkerboard structures depends on the regularization (i.e., smoothing and flattening) used in the inversion. Because our model spans a relatively wide region (55° in longitude or ∼2500 km), relatively high smoothing and flattening weights were applied in the inversion. Nonetheless, the 20–30% amplitude recovery achieved is within the range of previous studies using similar tomographic techniques (e.g., Watson et al., 2006).

7.2. Tabular body test

To further evaluate the resolution of anomalies in our model, we created a number of synthetic velocity structures, or tabular bodies, along profile A–A′ (Fig. 5). As with the checkerboard tests, we calculated associated travel times and inverted them to assess recoverability. For each tabular body, we specify a peak amplitude of the velocity anomaly, its length along-strike, its width, and the depth range over which the velocity anomaly tapers off, which we derive to be consistent with our final model (Fig. 3e). Fig. 5 shows the corresponding tabular body input model as well as the recovered structure obtained from inverting the synthetic travel times using the same parameterization as in our actual model. The recovered amplitudes of the tabular velocity anomalies are between 20–25% of the input, except for the anomaly beneath RI. Since the recovered synthetic anomaly beneath Ross Island is smaller than Anomaly G in our model (Fig. 3), this low V_P structure must either be relatively stronger or broader than our input tabular body. The recovered synthetic structure in the tabular test already extends deeper than Anomaly G in our model, suggesting a stronger, rather than a deeper, structure is present beneath Ross Island when compared to our input tabular body (Fig. 5). Another difference between the pattern in the recovered tabular test and our final model occurs within EA, where the recovered high V_P anomaly does not extend as deep as Anomaly I in our model (Figs. 3 and 5). This suggests that the input synthetic anomaly was either too weak or too shallow, implying that the peak amplitude of the fast structure beneath EA could be deeper than 100 km, the depth of the input body. Overall, the vertical smearing in the recovered synthetic tabular test is very similar to the model (Fig. 5c).

8. Discussion

The wide aperture of the combined seismic networks used in this study allows us to investigate relative variations in upper mantle structure beneath several Antarctic terranes within a single consistently referenced model. Previous regional body wave

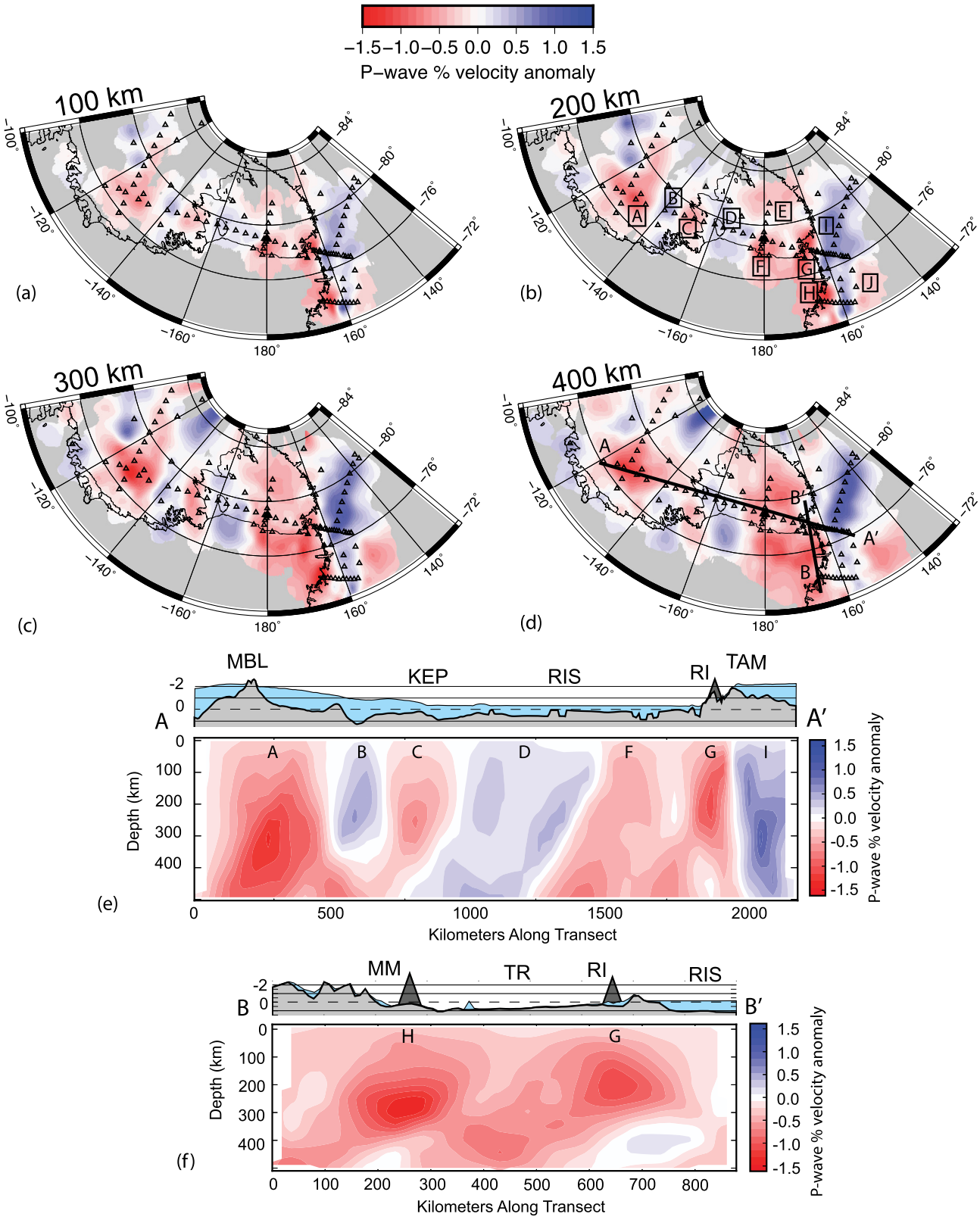

Fig. 3. a–d) Depth slices through P-wave model at 100 km increments. Triangles mark station locations. Anomalies A–J discussed in the text are labeled in (b). Black line segments in (d) denote lines of cross-section locations, shown in (e–f). e) Cross-section A–A′ through the tomography model, with bed and ice surface profiles above (from BEDMAP2; Fretwell et al., 2013). RIS: Ross Ice Shelf. Other abbreviations are the same as Fig. 1. Anomalies A–J discussed in text are labeled. Dark gray triangle marks Mt. Erebus on RI. f) Same as (e) but for cross-section B–B′. MM: Mt. Melbourne.

studies have identified heterogeneity within various regions in Antarctica, but making comparisons between terranes greater than 1000 km apart relative to the same model mean has been difficult. With the RIS/DRIS network connecting seismic stations in the TAM region to those in MBL and the central WARS, we can assess relative V_P variations between these provinces while si-

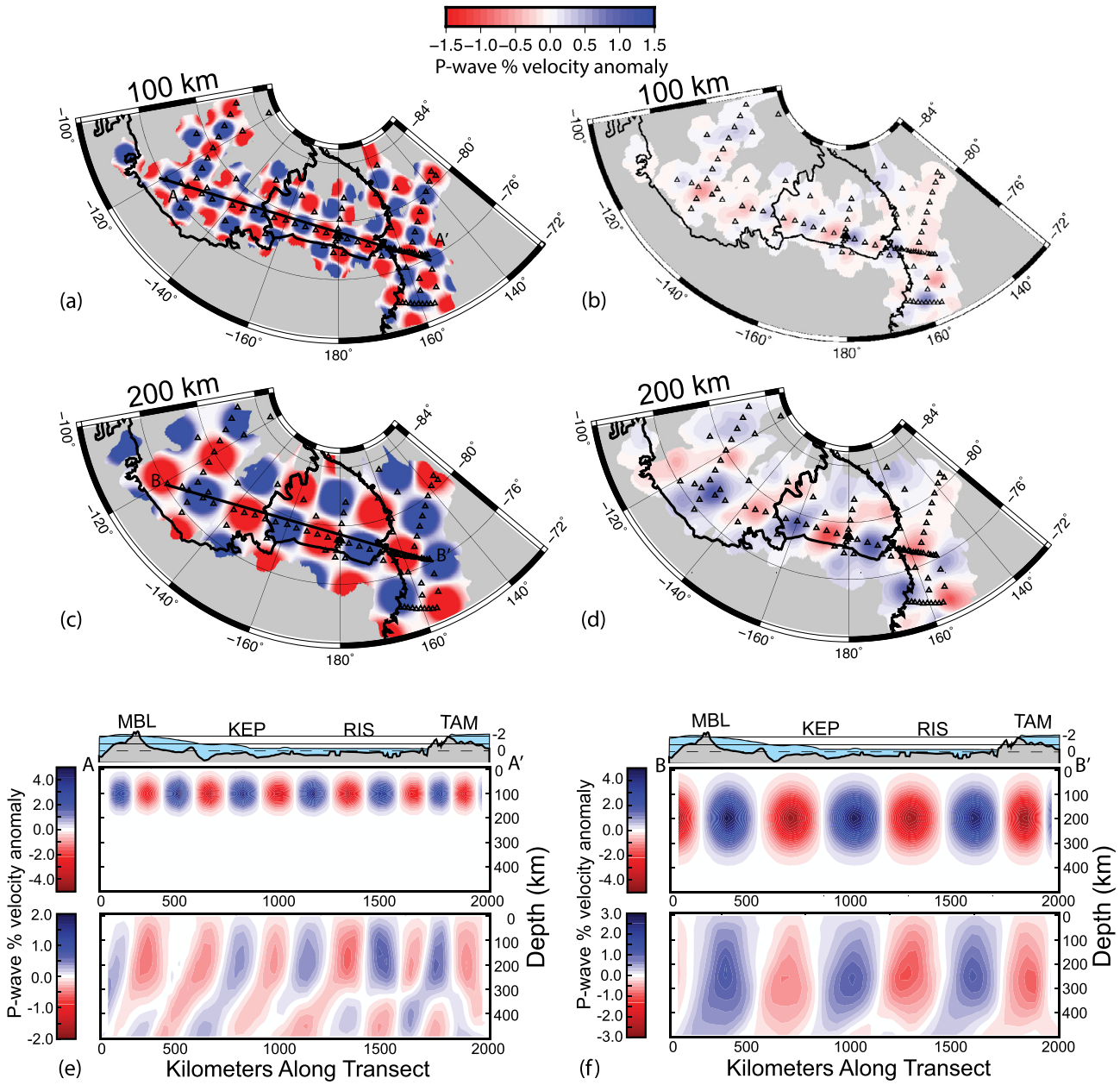

Fig. 4. a) Input synthetic model with 50 km radius Gaussian tapered spheres with peak amplitude of ±5% centered at 100 km depth. b) Corresponding recovered structure from (a). c) Input synthetic model with 100 km radius Gaussian tapered spheres centered at 200 km depth. d) Corresponding recovered structure from (c). e) Cross-section along A–A′ (Fig. 3) showing 50 km radius sphere input model from (a) on the upper panel and recovered model from (b) on the lower panel. f) Cross-section along B–B′ (Fig. 3) showing 100 km radius input model from (c) on the upper panel and recovered model from (d) on the lower panel.

multaneously focusing on the previously poorly resolved region of the RSE. Additionally, by including data from seismic stations in regions adjacent to the RSE, we can evaluate the consistency of our model with previous tomographic results (Watson et al., 2006; Brenn et al., 2017; Lawrence et al., 2006; Hansen et al., 2014; Lloyd et al., 2015; Heeszel et al., 2016; Shen et al., 2018).

Given the results of the tabular body tests (Fig. 5) and the limited resolution of our model below 300 km, we believe that anomalies present in our model, with the exception of Anomaly A in MBL (Fig. 3), arise primarily from heterogeneous structure within the lithospheric mantle. However, heterogeneous upper mantle structure may not necessarily be confined to the mantle lithosphere and could in some places extend below the lithosphere into the asthenosphere. While difficult to constrain, recent shear wave velocity models of West Antarctica (Shen et al., 2018; Heeszel et al., 2016) indicate a lithospheric thickness of ≥80–100 km for much of the RSE, 70–100 km for the central WARS, and 60–100 km in MBL.

Because a primary influence on V_P variability in the upper mantle is temperature (Cammarano et al., 2003), and, because geochemical analyses of Cenozoic mafic alkaline volcanic rocks across WA reveal a fairly narrow range of isotopic and trace element compositions (Hole and LeMasurier, 1994), we attribute the velocity variations in our model mainly to relative temperature differences. For calculations, we use the V_P temperature sensitivity (±0.75% per 100 °C) from Cammarano et al. (2003). Because of the ∼20–25% amplitude recovery in our resolution tests (see Figs. 4–5), this approach yields minimum temperature change estimates. Beneath MBL, however, water content in the upper mantle may be elevated compared to other areas of WA due to a history of subduction in the region (LeMasurier et al., 2016). Elevated pH2O could suppress the mantle solidus and lead to greater amounts of

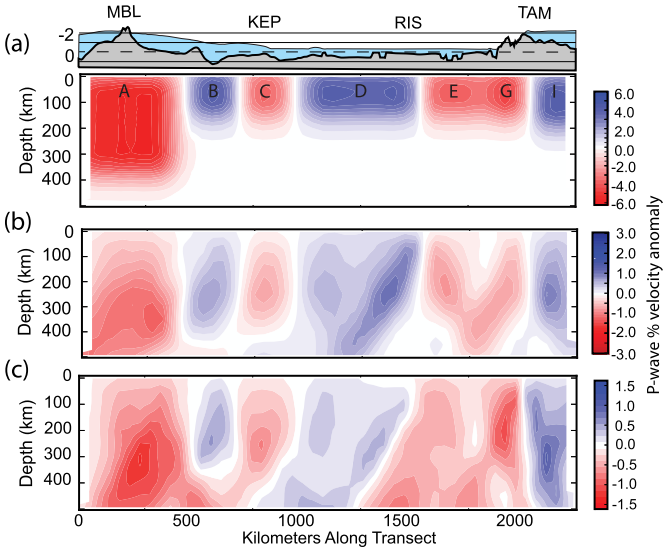

Fig. 5. a) Cross-section A–A′ (Fig. 3) with tabular body synthetic input. Anomalies discussed in the text are labeled. All input anomalies have ±4% peak amplitudes, except for the 50 km wide body directly beneath RI corresponding to Anomaly G, which has a −6% peak amplitude. b) Corresponding recovered anomalies. c) Cross-section through the actual model for comparison (same as Fig. 3e).

partial melt in the upper mantle. If this is happening, then upper mantle temperatures beneath MBL may not be as elevated as elsewhere in WA where we also image V_P anomalies of −1.5%.

Our model reveals heterogeneous structure not clearly seen in previous tomographic models of WA (e.g., Anomalies B and C). Faster V_P in Anomaly B underlying the Ford Ranges separates Anomaly C in the KEP area from Anomaly A beneath MBL, previously imaged and interpreted by Lloyd et al. (2015) and Hansen et al. (2014) as thermally perturbed upper mantle (Figs. 1 and 3b). Along cross-section A–A′ (Fig. 3e), it is difficult to ascertain whether Anomaly C connects to Anomaly A at depth because of the limited depth resolution of the model. The tabular body test (Fig. 5) suggests little to no connectivity between these two anomalies; however, there is some indication of connectivity between Anomalies A and C south of Anomaly B in the 400 km depth slice (Fig. 3d). Given the geographic proximity of Anomalies A and C, it seems possible that the mantle beneath the KEP could be influenced by thermochemically perturbed upper mantle structure beneath MBL but separated by less perturbed lithosphere beneath the Ford Ranges. While there are no known Cenozoic volcanoes in the KEP, the high geothermal heat flux (Maule et al., 2005) and seismic activity (Winberry and Anandakrishnan, 2003) found there could be linked to magmatic processes occurring in the region (Fig. 1b).

Within the RSE (Fig. 1), our model shows a clear dichotomy between faster, cooler upper mantle structure in the eastern RSE (Anomaly D) and slower, warmer upper mantle structure in the western RSE (Anomaly E; Fig. 3e). The difference in V_P between these regions indicates at least a ∼100 °C change in upper mantle temperature across the RSE. We attribute the temperature difference to the presence of colder and/or thicker lithosphere under the eastern RSE, in which case there may have been little, if any, Cenozoic reheating of the lithosphere in that part of the WARS. Spatially, Anomaly D correlates with the location of the Eastern Basin (Fig. 1c) (e.g., Decesari et al., 2007; Davey and Brancolini, 1995; Brancolini et al., 1995; and Granot et al., 2013), and extends beneath the interior of the Ross Ice Shelf (Fig. 6).

In the western RSE, our model shows three very low V_P anomalies (−1.25%; Anomalies F, G, and H) within a broader region of low V_P (−0.75%; Anomaly E). Anomalies G and H, which underlie the two active volcanoes Mt. Erebus and Mt. Melbourne along the TAM front (Fig. 6), are similar to the low velocity regions beneath these volcanoes imaged by Brenn et al. (2017). Anomaly F is located in the central RSE (Fig. 3). Bifurcation of the input anomaly in the tabular body test (Fig. 5) suggests that Anomaly F could simply be part of the broader Anomaly E. The dense cluster of DRIS stations in the central Ross Ice Shelf significantly increases ray density in this portion of the model (Supp. Fig. 4). Several iterations of the model were run with various station configurations, including the removal of all of the DRIS stations. While the bifurcated velocity pattern still persists when the DRIS stations are removed, the amplitude of Anomaly F approaches that of Anomaly E (Supp. Fig. 4), indicating that Anomaly F could be an artefact from high ray density. Because of that, we argue that the western RSE is primarily characterized by a broad region (∼500 km wide) of thermally perturbed lithosphere ($V_P \sim -0.75\%$), with focused lower V_P regions (−1.5%) along the TAM front under areas of recent magmatism (i.e., Anomalies G and H). The larger reduction (−1.5%) in P-wave velocities beneath these volcanoes suggests a further ∼100 °C increase in upper mantle temperatures and/or the presence of partial melt, which is consistent with the suggestion by Brenn et al. (2017) that partial melt, either within the lithosphere or ponded at its base, could be present.

The east-to-west change in the RSE upper mantle temperature, from the cooler temperatures beneath the Eastern Basin to the warmer temperatures beneath the western basins, to the even warmer temperatures and/or partially melted rock beneath Mt Erebus and Mt. Melbourne can be interpreted as evidence of multiple phases of rifting in the WARS. Broad-scale rifting during the Late

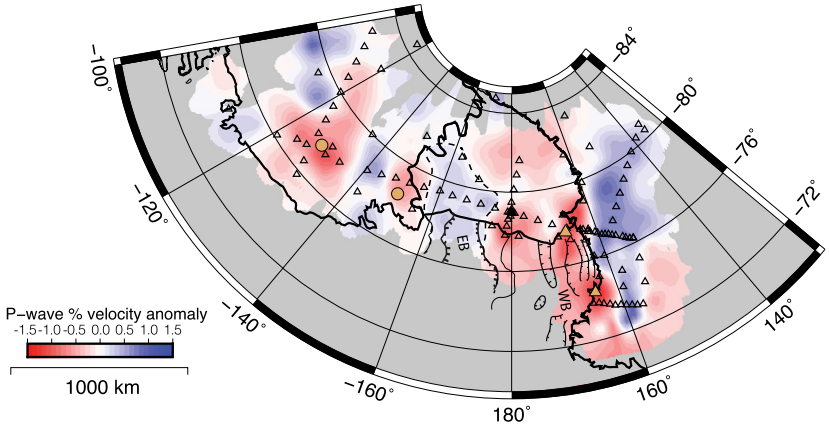

Fig. 6. Depth slice at 200 km through P-wave model (same as Fig. 3b), showing the eastern (EB) and western (WB) portions of the RSE, the locations of seismicity in MBL (orange circles), active volcanoes (orange triangles) and seismic stations (open triangles).

Cretaceous led to many of the extensional structures present in the RSE (i.e., thinned crust and rift basins; Siddoway, 2008). The relatively low seismic velocities across the western portion of the RSE, compared to the eastern portion, can be explained by a Paleogene phase of extension that resulted in thinning and warming of the lithosphere (Anomaly E) and regional transtensional deformation (Faccenna et al., 2008). An even younger (Neogene-Present) period of extension focused along the TAM front, associated with the development of the Terror Rift and alkaline shield volcanism, may have followed that phase of rifting, and was possibly influenced by plume processes in the mantle (Phillips et al., 2018; and references therein).

Away from the KEP and RSE, our model shows similar structures to previous body wave tomography models. For instance, our model shows a strong horizontal velocity contrast directly beneath the TAM. Watson et al. (2006) imaged similar structure and showed a 2–3% change in V_P over a lateral distance of ∼50–100 km, demarcating the sharp boundary between the EA and WA lithosphere. Further to the north beneath Northern Victoria Land, Brenn et al. (2017) modeled a similar velocity contrast (∼2–3%) beneath the TAM, marking an abrupt transition from WA to EA lithosphere.

Beneath the Wilkes Subglacial Basin, both our model and the Brenn et al. (2017) model show a velocity reduction in the upper mantle. Although the Wilkes Subglacial Basin is near the edge of the model, where model resolution degrades, we believe that the imaged velocity reduction is sufficiently resolved to suggest the presence of thermally perturbed lithospheric mantle and/or lithosphere that is thinner than the surrounding areas of EA, as suggested by aeromagnetic surveys (Ferraccioli et al., 2009).

In MBL, Lloyd et al. (2015) reported a 2–3% V_P variation in the upper mantle structure between the Executive Committee Range and adjacent areas, and attributed the velocity variation to a ∼150 °C thermal anomaly. However, as noted previously, if the MBL upper mantle has a higher water content than elsewhere in WA, the velocity variation could also be caused by an increase in partial melt and a thermal anomaly less than +150 °C. Hansen et al. (2014) also imaged a similar upper mantle low velocity structure beneath MBL. The location and amplitude of Anomaly A (Fig. 3) is consistent with the Lloyd et al. (2015) and Hansen et al. (2014) models. When taking vertical smearing into account, Anomaly A could be confined to the upper 400 km; however, given the limited vertical resolution in our model, we are not able to tightly constrain the depth extent of the anomaly. The tabular body test (Fig. 5) mimics Anomaly A in our model and requires that the input structure extend to at least 300 km depth, suggesting that the structure beneath MBL is present at sublithospheric depths but may not extend as deep as the transition zone. This suggestion is consistent with Emry et al. (2015), who show little evidence for thinning of the transition zone beneath MBL.

Our model is also broadly consistent with previous regional surface wave models that image upper mantle structure beneath MBL and the RSE. For example, both Heeszel et al. (2016) and Shen et al. (2018) show faster shear-wave velocities (V_S ∼ 4.5–4.6 km/s) down to ∼80 km depth within the Eastern Basin and parts of the central WARS, with slower V_S (∼4.2–4.3 km/s) at similar depths beneath the western basins. The variation in upper mantle V_S between the eastern and western basins is consistent with the variation in V_P in our model. The Shen et al. (2018) model also suggests slower upper mantle velocities beneath the KEP than the Ford Ranges at 80 km depth; however, the broad sensitivity kernels, wide Fresnel zones, and long wavelengths (∼300 km) of Rayleigh waves sensitive to structure at ∼100 km depth (Yang and Forsyth, 2006) make the KEP structure difficult to constrain using surface waves.

The heterogeneity in upper mantle V_P structure (∼ ±0.75%) present throughout much of WA has important implications for surface heat flow and upper mantle viscosity. The variability in the velocity structure suggests at least ±100 °C variations in upper mantle temperatures over length scales of 100 km and more. In steady state, lithospheric mantle temperature anomalies of ±100 °C would lead to ∼ ±10 mW/m^2 changes in surface heat flow. While this variability does not account for the large range in point estimates of heat flow across WA (e.g., 69 mW/m^2, Engelhardt, 2004; 115 mW/m^2, Morin et al., 2010; and 285 mW/m^2, Fisher et al., 2015), it is consistent with the variability in regional heat flow (Schroeder et al., 2014; Maule et al., 2005; Pollard et al., 2005), and may be large enough to affect basal ice conditions. With regard to mantle viscosity, O'Donnell et al. (2017) showed that ±100 °C temperature variations in the upper mantle can result in viscosity changes of ∼2 orders of magnitude, which Barletta et al. (2018) argued can have a significant impact on ice sheet stability by influencing glacial isostatic adjustment.

9. Summary and conclusions

A P-wave model of upper mantle structure, extending from MBL and the WARS into EA, has been generated by inverting 32,454 relative P-wave travel-time residuals recorded by the RIS/DRIS and other Antarctic seismic networks. The model has improved resolution over previously published body wave models for the region, particularly within the RSE sector of the WARS.

Within the RSE, our model shows a clear dichotomy in the upper mantle velocity structure between the eastern and western basins. Seismically fast upper mantle beneath the eastern RSE correlates with the Eastern Basin and suggests that the lithosphere in this region may not have been reheated by Cenozoic rifting. Seismically slow upper mantle over a ∼500 km-wide area beneath the western RSE transitions to more focused, ∼100 km-wide regions of even slower velocity along the TAM front beneath Mt. Erebus and Mt. Melbourne. We attributed the broad slow velocity region beneath the western RSE to Paleogene rifting, while the focused slower velocity anomalies under Mt. Erebus and Mt. Melbourne could be associated with a Neogene-Present phase of rifting and/or plume activity, which created the Terror Rift. Within the Ford Ranges and KEP in western MBL, we also see significant lateral variability in upper mantle velocity structure (±0.50%) over distances of only a few hundred km.

The heterogeneity in upper mantle velocity structure in our model, assuming no significant variation in composition, represents changes in temperature of at least 100 °C over distances of hundreds of km. This variability in mantle temperature could lead to surface heat flow variations of ∼ ±10 mW/m^2 and 10^2 Pa s changes in mantle viscosity, which could influence the stability of the West Antarctic Ice Sheet by affecting basal ice conditions and glacial isostatic adjustment.

Acknowledgements

This work was supported by the National Science Foundation (NSF) (grants 1142126, 1142518, 1141916, 1148982, 1246416, 1246151, 1249631, 1249602, 1249513, 1246666, 1246712, 1246776, 1247518). The seismic deployments in this study benefited greatly from the technical support of the Incorporated Research Institutions for Seismology (IRIS) through the Portable Array Seismic Studies of the Continental Lithosphere (PASSCAL) Instrument Center at New Mexico Tech. Seismic data are freely available through the IRIS Data Management Center. We thank Patrick Shore for providing invaluable support in collecting and archiving data from all of the projects, as well as Anya Reading and two anonymous reviewers for constructive reviews. Many of the figures were made using the freely available Generic Mapping Tools software (Wessel et al., 2013).

Appendix A. Supplementary material

Supplementary material related to this article can be found online at https://doi.org/10.1016/j.epsl.2019.02.013.

References

Barletta, V.R., Bevis, M., Smith, B.E., Wilson, T.J., Brown, A., Bordoni, A., Willis, M., Khan, S.A., Rovira-Navarro, M., Dalziel, I.W., Smalley Jr., R., Kendrick, E., Konfal, S., Caccamise, D.J., Aster, R.C., Nyblade, A.A., Wiens, D.A., 2018. Observed rapid bedrock uplift in Amundsen Sea Embayment promotes ice-sheet stability. Science 360 (6395), 1335–1339. https://doi.org/10.1126/science.aao1447.

Behrendt, J.C., Saltus, R., Damaske, D., McCafferty, A., Finn, C.A., Blankenship, D., Bell, R.E., 1996. Patterns of late Cenozoic volcanic and tectonic activity in the West Antarctic rift system revealed by aeromagnetic surveys. Tectonics 15 (3), 660–676. https://doi.org/10.1029/95tc03500.

Brancolini, G., Cooper, A.K., Coren, F., 1995. Seismic facies and glacial history in the western Ross Sea (Antarctica). In: Geology and Seismic Stratigraphy of the Antarctic Margin, pp. 209–233.

Brenn, G.R., Hansen, S.E., Park, Y., 2017. Variable thermal loading and flexural uplift along the Transantarctic Mountains, Antarctica. Geology 45 (5), 463–466. https://doi.org/10.1130/g38784.1.

Cammarano, F., Goes, S., Vacher, P., Giardini, D., 2003. Inferring upper-mantle temperatures from seismic velocities. Phys. Earth Planet. Inter. 138 (3–4), 197–222. https://doi.org/10.1016/s0031-9201(03)00156-0.

Chaput, J., Aster, R.C., Huerta, A., Sun, X., Lloyd, A.D., Wiens, D., Nyblade, A.A., Anandakrishnan, S., Winberry, J.P., Wilson, T., 2014. The crustal thickness of West Antarctica. J. Geophys. Res., Solid Earth 119 (1), 378–395. https://doi.org/10.1002/2013jb010642.

Dalziel, I.W., Elliot, D.H., 1982. West Antarctica: problem child of Gondwanaland. Tectonics 1 (1), 3–19. https://doi.org/10.1029/tc001i001p00003.

Danesi, S., Morelli, A., 2001. Structure of the upper mantle under the Antarctic Plate from surface wave tomography. Geophys. Res. Lett. 28 (23), 4395–4398. https://doi.org/10.1029/2001gl013431.

Davey, F.J., 1981. Geophysical studies in the Ross Sea region. J. R. Soc. N. Z. 11 (4), 465–479. https://doi.org/10.1080/03036758.1981.10423336.

Davey, F.J., Brancolini, G., 1995. The Late Mesozoic and Cenozoic structural setting of the Ross Sea region. In: Geology and Seismic Stratigraphy of the Antarctic Margin, pp. 167–182.

Decesari, R.C., Wilson, D.S., Luyendyk, B.P., Faulkner, M., 2007. Cretaceous and tertiary extension throughout the Ross Sea, Antarctica. In: Cooper, A.K., et al. (Eds.), Antarctica: A Keystone in a Changing World – Online Proceedings of the 10th ISAES X. U.S. Geological Survey Open File Rep., 1047.

Emry, E.L., Nyblade, A.A., Julià, J., Anandakrishnan, S., Aster, R.C., Wiens, D.A., Huerta, A.D., Wilson, T.J., 2015. The mantle transition zone beneath West Antarctica: seismic evidence for hydration and thermal upwellings. Geochem. Geophys. Geosyst. 16 (1), 40–58. https://doi.org/10.1002/2014gc005588.

Engelhardt, H., 2004. Ice temperature and high geothermal flux at Siple Dome, West Antarctica, from borehole measurements. J. Glaciol. 50 (169), 251–256. https://doi.org/10.3189/172756504781830105.

Faccenna, C., Rossetti, F., Becker, T.W., Danesi, S., Morelli, A., 2008. Recent extension driven by mantle upwelling beneath the Admiralty Mountains (East Antarctica). Tectonics 27 (4). https://doi.org/10.1029/2007TC002197.

Ferraccioli, F., Armadillo, E., Jordan, T., Bozzo, E., Corr, H., 2009. Aeromagnetic exploration over the East Antarctic Ice Sheet: a new view of the Wilkes Subglacial Basin. Tectonophysics 478 (1–2), 62–77. https://doi.org/10.1016/j.tecto.2009.03.013.

Fielding, C.R., Henrys, S.A., Wilson, T.J., 2006. Rift history of the western Victoria Land Basin: a new perspective based on integration of cores with seismic reflection data. Antarctica 309 (318). https://doi.org/10.1007/3-540-32934-x_39.

Finn, C.A., Müller, R.D., Panter, K.S., 2005. A Cenozoic diffuse alkaline magmatic province (DAMP) in the southwest Pacific without rift or plume origin. Geochem. Geophys. Geosyst. 6 (2). https://doi.org/10.1029/2004GC000723.

Fisher, A.T., Mankoff, K.D., Tulaczyk, S.M., Tyler, S.W., Foley, N., 2015. High geothermal heat flux measured below the West Antarctic Ice Sheet. Sci. Adv. 1 (6), e1500093. https://doi.org/10.1126/sciadv.1500093.

Fitzgerald, P.G., 1992. The Transantarctic Mountains of southern Victoria Land: the application of apatite fission track analysis to a rift shoulder uplift. Tectonics 11 (3), 634–662. https://doi.org/10.1029/91tc02495.

Fitzgerald, P.G., 2002. Tectonics and landscape evolution of the Antarctic plate since the breakup of Gondwana, with an emphasis on the West Antarctic Rift System and the Transantarctic Mountains. Bull. R. Soc. N. Z. 35, 453–469. DOI.

Fretwell, P., Pritchard, H.D., Vaughan, D.G., Bamber, J.L., Barrand, N.E., Bell, R., Bianchi, C., Bingham, R.G., Blankenship, D.D., Casassa, G., Catania, G., 2013. Bedmap2: improved ice bed, surface and thickness datasets for Antarctica. https://doi.org/10.5194/tcd-6-4305-2012.

Gomez, N., Pollard, D., Holland, D., 2015. Sea-level feedback lowers projections of future Antarctic Ice-Sheet mass loss. Nat. Commun. 6, 8798. https://doi.org/10.1038/ncomms9798.

Granot, R., Cande, S.C., Stock, J.M., Damaske, D., 2013. Revised Eocene–Oligocene kinematics for the West Antarctic rift system. Geophys. Res. Lett. 40 (2), 279–284. https://doi.org/10.1029/2012gl054181.

Graw, J.H., Adams, A.N., Hansen, S.E., Wiens, D.A., Hackworth, L., Park, Y., 2016. Upper mantle shear wave velocity structure beneath northern Victoria Land, Antarctica: volcanism and uplift in the northern Transantarctic Mountains. Earth Planet. Sci. Lett. 449, 48–60. https://doi.org/10.1016/j.epsl.2016.05.026.

Hansen, S.E., Graw, J.H., Kenyon, L.M., Nyblade, A.A., Wiens, D.A., Aster, R.C., Huerta, A.D., Anandakrishnan, S., Wilson, T.J., 2014. Imaging the Antarctic mantle using adaptively parameterized P-wave tomography: evidence for heterogeneous structure beneath West Antarctica. Earth Planet. Sci. Lett. 408, 66–78. https://doi.org/10.1016/j.epsl.2014.09.043.

Heeszel, D.S., Wiens, D.A., Anandakrishnan, S., Aster, R.C., Dalziel, I.W., Huerta, A.D., Nyblade, A.A., Wilson, T.J., Winberry, J.P., 2016. Upper mantle structure of central and West Antarctica from array analysis of Rayleigh wave phase velocities. J. Geophys. Res., Solid Earth 121 (3), 1758–1775. https://doi.org/10.1002/2015jb012616.

Hole, M.J., LeMasurier, W.E., 1994. Tectonic controls on the geochemical composition of Cenozoic, mafic alkaline volcanic rocks from West Antarctica. Contrib. Mineral. Petrol. 117 (2), 187–202. https://doi.org/10.1007/BF00286842.

Karner, G.D., Studinger, M., Bell, R.E., 2005. Gravity anomalies of sedimentary basins and their mechanical implications: application to the Ross Sea basins, West Antarctica. Earth Planet. Sci. Lett. 235 (3–4), 577–596. https://doi.org/10.1016/j.epsl.2005.04.016.

Kennett, B.L.N., Engdahl, E.R., 1991. Traveltimes for global earthquake location and phase identification. Geophys. J. Int. 105 (2), 429–465. https://doi.org/10.1111/j.1365-246x.1991.tb06724.x.

Lawrence, J.F., Wiens, D.A., Nyblade, A.A., Anandakrishnan, S., Shore, P.J., Voigt, D., 2006. Crust and upper mantle structure of the Transantarctic Mountains and surrounding regions from receiver functions, surface waves, and gravity: implications for uplift models. Geochem. Geophys. Geosyst. 7 (10). https://doi.org/10.1029/2006gc001282.

LeMasurier, W.E., 1990. Late Cenozoic volcanism on the Antarctic plate: an overview. In: Volcanoes of the Antarctic Plate and Southern Oceans, vol. 48, pp. 1–17.

LeMasurier, W.E., Choi, S.H., Hart, S.R., Mukasa, S., Rogers, N., 2016. Reconciling the shadow of a subduction signature with rift geochemistry and tectonic environment in Eastern Marie Byrd Land, Antarctica. Lithos 260, 134–153. https://doi.org/10.1016/j.lithos.2016.05.018.

LeMasurier, W.E., Landis, C.A., 1996. Mantle-plume activity recorded by low-relief erosion surfaces in West Antarctica and New Zealand. Geol. Soc. Am. Bull. 108 (11), 1450–1466. https://doi.org/10.1130/0016-7606(1996)108<1450:MPARBL>2.3.CO;2.

Lloyd, A.J., Wiens, D.A., Nyblade, A.A., Anandakrishnan, S., Aster, R.C., Huerta, A.D., Wilson, T.J., Dalziel, I.W., Shore, P.J., Zhao, D., 2015. A seismic transect across West Antarctica: evidence for mantle thermal anomalies beneath the Bentley Subglacial Trench and the Marie Byrd Land Dome. J. Geophys. Res., Solid Earth 120 (12), 8439–8460. https://doi.org/10.1002/2015jb012455.

Lough, A.C., Wiens, D.A., Barcheck, C.G., Anandakrishnan, S., Aster, R.C., Blankenship, D.D., Huerta, A.D., Nyblade, A.A., Young, D.A., Wilson, T.J., 2013. Seismic detection of an active subglacial magmatic complex in Marie Byrd Land, Antarctica. Nat. Geosci. 6 (12), 1031. https://doi.org/10.1038/ngeo1992.

Masters, G., Johnson, S., Laske, G., Bolton, H., 1996. A shear-velocity model of the mantle. Philos. Trans. R. Soc. Lond. A 354 (1711), 1385–1411. https://doi.org/10.1098/rsta.1996.0054.

Maule, C.F., Purucker, M.E., Olsen, N., Mosegaard, K., 2005. Heat flux anomalies in Antarctica revealed by satellite magnetic data. Science 309 (5733), 464–467. https://doi.org/10.1126/science.1106888.

Morin, R.H., Williams, T., Henrys, S.A., Magens, D., Niessen, F., Hansaraj, D., 2010. Heat flow and hydrologic characteristics at the AND-1B borehole, ANDRILL McMurdo Ice Shelf Project, Antarctica. Geosphere 6 (4), 370–378. https://doi.org/10.1130/ges00512.1.

Mukasa, S.B., Dalziel, I.W., 2000. Marie Byrd Land, West Antarctica: evolution of Gondwana's Pacific margin constrained by zircon U–Pb geochronology and feldspar common-Pb isotopic compositions. Geol. Soc. Am. Bull. 112 (4), 611–627. https://doi.org/10.1130/0016-7606(2000)112<611:mblwae>2.0.co;2.

O'Donnell, J.P., Selway, K., Nyblade, A.A., Brazier, R.A., Wiens, D.A., Anandakrishnan, S., Aster, R.C., Huerta, A.D., Wilson, T.J., Winberry, J.P., 2017. The uppermost mantle seismic velocity and viscosity structure of central West Antarctica. Earth Planet. Sci. Lett. 472, 38–49. https://doi.org/10.1016/j.epsl.2017.05.016.

Phillips, E.H., Sims, K.W., Blichert-Toft, J., Aster, R.C., Gaetani, G.A., Kyle, P.R., Wallace, P.J., Rasmussen, D.J., 2018. The nature and evolution of mantle upwelling at Ross Island, Antarctica, with implications for the source of HIMU lavas. Earth Planet. Sci. Lett. 498, 38–53. https://doi.org/10.1016/j.epsl.2018.05.049.

Pollard, D., DeConto, R.M., Nyblade, A.A., 2005. Sensitivity of Cenozoic Antarctic ice sheet variations to geothermal heat flux. Glob. Planet. Change 49 (1–2), 63–74. https://doi.org/10.1016/j.gloplacha.2005.05.003.

Ramirez, C., Nyblade, A., Emry, E.L., Julià, J., Sun, X., Anandakrishnan, S., Wiens, D.A., Aster, R.C., Huerta, A.D., Winberry, P., Wilson, T., 2017. Crustal structure of the Transantarctic Mountains, Ellsworth Mountains and Marie Byrd Land, Antarctica: constraints on shear wave velocities, Poisson's ratios and Moho depths. Geophys. J. Int. 211 (3), 1328–1340. https://doi.org/10.1093/gji/ggx333.

Ramirez, C., Nyblade, A., Hansen, S.E., Wiens, D.A., Anandakrishnan, S., Aster, R.C., Huerta, A.D., Shore, P., Wilson, T., 2016. Crustal and upper-mantle structure beneath ice-covered regions in Antarctica from S-wave receiver functions and implications for heat flow. Geophys. J. Int. 204 (3), 1636–1648. https://doi.org/10.1093/gji/ggv542.

Rignot, E., Bamber, J.L., Van Den Broeke, M.R., Davis, C., Li, Y., Van De Berg, W.J., Van Meijgaard, E., 2008. Recent Antarctic ice mass loss from radar interferometry and regional climate modelling. Nat. Geosci. 1 (2), 106. https://doi.org/10.1038/ngeo102.

Ritzwoller, M.H., Shapiro, N.M., Levshin, A.L., Leahy, G.M., 2001. Crustal and upper mantle structure beneath Antarctica and surrounding oceans. J. Geophys. Res., Solid Earth 106 (B12), 30645–30670. https://doi.org/10.1029/2001jb000179.

Roult, G., Rouland, D., Montagner, J.P., 1994. Antarctica II: upper-mantle structure from velocities and anisotropy. Phys. Earth Planet. Inter. 84 (1–4), 33–57. https://doi.org/10.1016/0031-9201(94)90033-7.

Schroeder, D.M., Blankenship, D.D., Young, D.A., Quartini, E., 2014. Evidence for elevated and spatially variable geothermal flux beneath the West Antarctic Ice Sheet. Proc. Natl. Acad. Sci. 111 (25), 9070–9072. https://doi.org/10.1073/pnas.1405184111.

Shen, W., Wiens, D., Anandakrishnan, A., Aster, R.C., Gerstoft, P., Bromirski, P., Hansen, S.E., Dalziel, I., Heeszel, D., Huerta, A., Nyblade, A.A., Stephen, R., Wilson, T., Winberry, J.P., 2018. The crust and upper mantle structure of central and West Antarctica from Bayesian inversion of Rayleigh wave and receiver functions. J. Geophys. Res. 123. https://doi.org/10.1029/2017JB015346.

Siddoway, C.S., 2008. Tectonics of the West Antarctic Rift System: new light on the history and dynamics of distributed intracontinental extension. In: Antarctica: A Keystone in a Changing World, pp. 91–114.

Sieminski, A., Debayle, E., Lévêque, J.J., 2003. Seismic evidence for deep low-velocity anomalies in the transition zone beneath West Antarctica. Earth Planet. Sci. Lett. 216 (4), 645–661. https://doi.org/10.1016/s0012-821x(03)00518-1.

Trey, H., Cooper, A.K., Pellis, G., della Vedova, B., Cochrane, G., Brancolini, G., Makris, J., 1999. Transect across the West Antarctic rift system in the Ross Sea, Antarctica. Tectonophysics 301 (1–2), 61–74. https://doi.org/10.1016/s0040-1951(98)00155-3.

VanDecar, J.C., 1991. Upper-Mantle Structure of the Cascadia Subduction Zone from Non-Linear Teleseismic Travel-Time Inversion (Doctoral dissertation).

VanDecar, J.C., Crosson, R.S., 1990. Determination of teleseismic relative phase arrival times using multi-channel cross-correlation and least squares. Bull. Seismol. Soc. Am. 80 (1), 150–169.

Watson, T., Nyblade, A., Wiens, D.A., Anandakrishnan, S., Benoit, M., Shore, P.J., Voigt, D., VanDecar, J., 2006. P and S velocity structure of the upper mantle beneath the Transantarctic Mountains, East Antarctic craton, and Ross Sea from travel time tomography. Geochem. Geophys. Geosyst. 7 (7). https://doi.org/10.1029/2005gc001238.

Wessel, P., Smith, W.H.F., Scharroo, R., Luis, J.F., Wobbe, F., 2013. Generic Mapping Tools: improved version released. Eos 94, 409–410. https://doi.org/10.1002/2013EO450001.

Winberry, J.P., Anandakrishnan, S., 2003. Seismicity and neotectonics of West Antarctica. Geophys. Res. Lett. 30 (18). https://doi.org/10.1029/2003gl018001.

Yang, Y., Forsyth, D.W., 2006. Regional tomographic inversion of the amplitude and phase of Rayleigh waves with 2-D sensitivity kernels. Geophys. J. Int. 166 (3), 1148–1160. https://doi.org/10.1111/j.1365-246X.2006.02972.x.